SU(4) Skyrmions in the $\nu = \pm 1$ Quantum Hall State of Graphene

Y. Lian,[1] A. Rosch,[2] and M. O. Goerbig[1]
[1]Laboratoire de Physique des Solides, Univ. Paris-Sud, Université Paris-Saclay, CNRS, UMR 8502, F-91405 Orsay Cedex, France
[2]Institut für Theoretische Physik, Universität zu Köln, D-50937 Cologne, Germany
(Received 19 February 2016; published 29 July 2016)

We explore different Skyrmion types in the lowest Landau level of graphene at a filling factor $\nu = \pm 1$. In addition to the formation of spin and valley pseudospin Skyrmions, we show that another type of spin-valley entangled Skyrmions can be stabilized in graphene due to an approximate SU(4) spin-valley symmetry that is affected by sublattice symmetry-breaking terms. These Skyrmions have a clear signature in spin-resolved density measurements on the lattice scale, and we discuss the expected patterns for the different Skyrmion types.

DOI: 10.1103/PhysRevLett.117.056806

Originally proposed in the framework of nuclear physics [1], Skyrmions have found physical reality in condensed-matter systems as topological textures of two-dimensional (2D) ferromagnets (FMs). Probably its conceptually purest form is realized in 2D electrons in a strong magnetic field B [2]—since their kinetic energy is quenched into highly degenerate Landau levels (LLs), all electrons spontaneously align their spins to minimize their Coulomb energy when there are as many electrons in a single LL as flux quanta threading the system. In the lowest LL, this corresponds to a filling factor $\nu = 1$, whereas in graphene the same situation is encountered also at $\nu = -1$, due to particle-hole symmetry [3,4]. In both systems, Skyrmions carry an electric charge given by their winding and have a lower energy than simple spin-flip excitations. In GaAs heterostructures, Skyrmion formation yields a rapid decay of the magnetization in the vicinity of $\nu = 1$, as measured in NMR experiments [5]. More recently, Skyrmions have regained interest [6] after their discovery in chiral magnets [7] and thin magnetic layers on heavy-metal substrates [8]. They are promising candidates for spintronics application as they can easily be manipulated by ultrasmall currents [9]. While characterized by the same type of winding numbers, Skyrmions in these materials differ from quantum Hall Skyrmions since they are bosonic quasiparticles and do not carry a quantized charge [10].

A promising material that combines the conceptual simplicity of quantum Hall (QH) systems and the direct accessibility as a surface material is graphene. Moreover, graphene is characterized by an additional pseudospin reflecting the two relevant valleys for its low-energy electronic properties [3]. Since the Coulomb energy respects to great accuracy this pseudospin symmetry [4], one encounters a particular form of SU(4) *ferromagnetism* [11–13] that allows for a much richer variety of Skyrmions involving the valley pseudospin. Although valley Skyrmions have been studied in other materials [14], the identity between valley and sublattice in the central $n = 0$ LL [4] makes graphene an ideal candidate for a direct measurement of valley Skyrmions, e.g., within spin-resolved scanning tunneling spectroscopy (STS). Because all electrons of a particular valley thus reside on a single sublattice, the valley pseudospin can be directly visualized by the sublattice occupation. This would allow for a direct measurement of pseudospin Skyrmions that are, e.g., depicted in Fig. 1 and their size as a function of B.

In this Letter, we illustrate the different Skyrmion types in graphene at $\nu = \pm 1$. Beyond the expected spin and pseudospin Skyrmions, we find a phase diagram with highly unusual Skyrmions with spin and pseudospin entanglement. Whereas such Skyrmions naturally arise in a purely SU(4)- [11,13], or more generally in any

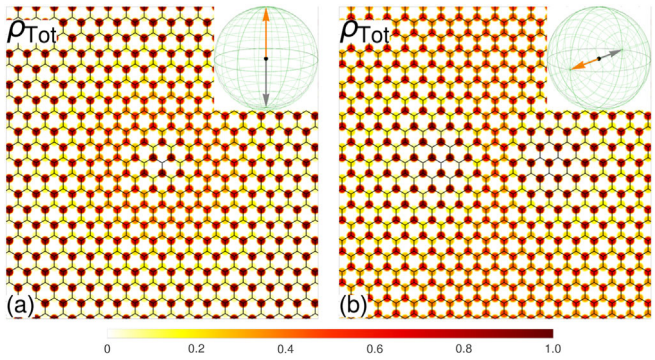

FIG. 1. Pseudospin Skyrmions in an easy-axis [(a)] and an easy-plane pseudospin [(b)] FM background. The two subfigures sketch the lattice-resolved total electronic density ρ_{tot} in the $n = 0$ LL. The insets show the pseudospin Bloch sphere, which is entirely covered. In each Bloch sphere, the orange and gray arrows show the polarization of the FM background at $r \to \infty$ and in the center, respectively. At intermediate values of r, all other parts of the Bloch sphere are explored. The spin (not shown) is homogeneously polarized. For illustration, we have used much smaller Skyrmion sizes (on the order of some lattice spacings) than encountered in an experimental situation (see text). Panels (a) and (b) correspond to points 3 and 2 in Fig. 2, respectively.

SU(K)-symmetric model [15], their occurrence in symmetry-broken situations has remained an open issue. Apart from a theoretical classification of the different Skyrmion types in terms of Bloch spheres, we show how these Skyrmions can be identified by their spin- and lattice-resolved electronic densities. Such densities are precisely accessible in STS, and our results may therefore be a guide in the spectroscopic identification of the different Skyrmions in graphene, beyond spin Skyrmions in the above-mentioned other systems.

Our study is based on the nonlinear σ model

$$E[Z(\mathbf{r})] = E_{\mathrm{SU}(4)}[Z(\mathbf{r})] + E_{\mathrm{SB}}[Z(\mathbf{r})] \tag{1}$$

in terms of the spatially varying CP^3 field [11,15–17]

$$Z(\mathbf{r}) = [\upsilon_{K\uparrow}(\mathbf{r}), \upsilon_{K\downarrow}(\mathbf{r}), \upsilon_{K'\uparrow}(\mathbf{r}), \upsilon_{K'\downarrow}(\mathbf{r})]^T, \tag{2}$$

whose four complex components represent the spin and pseudospin amplitudes in $n = 0$, and $\mathbf{r} = (x, y)$ is the planar coordinate. Its first term is SU(4) symmetric,

$$E_{\mathrm{SU}(4)}[Z(\mathbf{r})] = 2\rho_S \int d^2r \mathbf{D}Z^\dagger(\mathbf{r}) \cdot \mathbf{D}Z(\mathbf{r}) + \frac{1}{2}\int d^2r d^2r' \rho_{\mathrm{topo}}(\mathbf{r}) V(\mathbf{r}-\mathbf{r}') \rho_{\mathrm{topo}}(\mathbf{r}'), \tag{3}$$

with the spin stiffness $\rho_S = e^2/16\sqrt{2\pi}\epsilon l_B$ [2,18], the gradient $\mathbf{D}Z = \boldsymbol{\nabla} Z(\mathbf{r}) - [Z^\dagger(\mathbf{r})\boldsymbol{\nabla} Z(\mathbf{r})]Z(\mathbf{r})$, and the magnetic length $l_B = \sqrt{\hbar/eB}$. The second term is the Coulomb interaction $V(\mathbf{r}) = e^2/\epsilon|\mathbf{r}|$ between the charge-density fluctuations that are, at $\nu = \pm 1$, identical to the topological charge density $\rho_{\mathrm{topo}}(\mathbf{r}) = -(i/2\pi)[\mathbf{D}Z(\mathbf{r})^\dagger \times \mathbf{D}Z(\mathbf{r})]_z$ [18,19]. Apart from the SU(4) symmetric term, the model also hosts symmetry-breaking terms,

$$E_{\mathrm{SB}}[Z(\mathbf{r})] = \frac{\Delta_Z}{2}\int \frac{d^2r}{2\pi l_B^2}[u_\perp(P_x^2 + P_y^2) + u_z P_z^2 - S_z], \tag{4}$$

with the spin and pseudospin magnetizations

$$\mathbf{S} = Z^\dagger(\mathbf{r})(1 \otimes \sigma)Z(\mathbf{r}), \qquad \mathbf{P} = Z^\dagger(\mathbf{r})(\sigma \otimes 1)Z(\mathbf{r}), \tag{5}$$

respectively, where $\sigma = (\sigma_x, \sigma_y, \sigma_z)$ combines the three Pauli matrices. (An explicit expression of the spin and pseudospin densities, in terms of the CP^3-field components can be found in the Supplemental Material [20].) The parameters u_z and $u_\perp$, which are presented in units of the Zeeman energy Δ_Z, describe, e.g., the pseudospin-symmetry breaking due to out-of-plane [21] or in-plane [22] lattice distortions, or a symmetry breaking of the interaction at the lattice scale [12], and have been estimated to be all on the order of 0.1–0.2 meV $\times B[T]$, while the Zeeman effect is in the same range $\Delta_Z \simeq 0.1$ meV $\times B[T]$. For realistic magnetic fields, this is much smaller than the leading (interaction) energy scale $\rho_S \sim e^2/\epsilon l_B \simeq 50$ meV$\times \sqrt{B[T]}/\epsilon$. However, we emphasize that while the hierarchy of energy scales is well corroborated, the precise values of u_z and $u_\perp$ are unknown and are likely to depend on the substrate. We therefore use them as phenomenological parameters in our study.

Because at large distances from their center, Skyrmions approach the underlying FM background state, let us first discuss the phase diagram of homogeneous FM states described by a normalized spinor $Z(\mathbf{r}) = F$, similarly to Refs. [23] and [24] at $\nu = 0$. These states minimize the leading SU(4)-symmetric energy functional (3), $E_{\mathrm{SU}(4)} = 0$, since all gradient terms vanish, and the symmetry-breaking terms (4) thus determine the FM phase diagram (Fig. 2). Since the Zeeman term acts solely on the spin, and spin and pseudospin magnetic orders coexist at $\nu = \pm 1$, all phases display a homogeneous spin magnetization in the z direction. For $u_z \le 1/2$ or $u_\perp \le 1/2$, the spin and pseudospin magnetizations are disentangled, and one obtains an easy-plane pseudospin FM, with, e.g., $F = (1, 0, \pm 1, 0)^T/\sqrt{2}$, for $u_z > u_\perp$ and an easy-axis pseudospin FM, with $F = (1,0,0,0)^T$ or $F = (0, 0, 1, 0)^T$, for $u_z < u_\perp$, in addition to a full spin polarization. We stress that in $n = 0$ valley and sublattice are identical in the sense that the wave functions of an electron in a specific valley have only components on a particular sublattice [20]. The easy-axis pseudospin FM therefore takes the form of a charge-density wave with all spin-polarized electrons

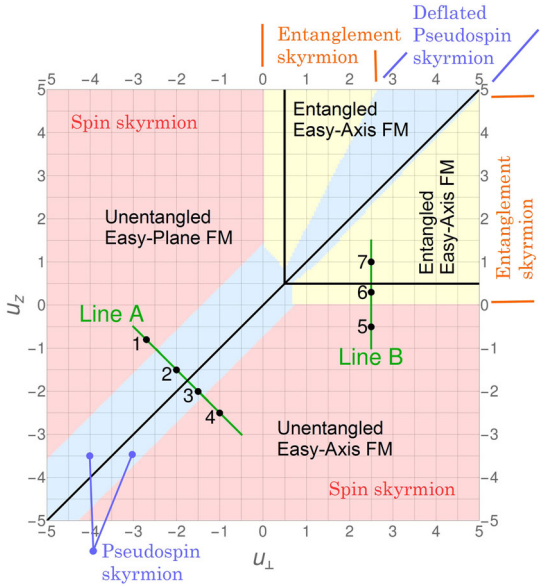

FIG. 2. Phase diagram of $\mathcal{Q} = 1$ Skyrmions (labeled in red, blue, and yellow) and the pseudospin FM background state (sketched in black), as a function of u_z and $u_\perp$ (in units of the Zeeman energy Δ_Z). The parameters used correspond to a field $B = 10$ T.

localized on a single sublattice, whereas both sublattices are equally populated in an easy-plane pseudospin FM.

The most interesting phases are obtained for u_z, $u_\perp > 1/2$ where the spin and pseudospin magnetizations are partially entangled due to energetic frustration. According to Eq. (4), the pseudospin contribution to the anisotropy energy is lowered when all components of the pseudospin magnetization are minimized. As an extreme case, we consider a superposition $F = (1, 0, 0, 1)/\sqrt{2}$ with spin-up electrons on the A sublattice and spin-down particles on the B sublattice, such that $\mathbf{P} = \mathbf{0}$. Somewhat counterintuitively, this state whose spin-density pattern is *antiferromagnetic* remains a particular SU(4) *FM* since it can be obtained from a pure spin (and pseudospin) FM via a rotation in the SU(4) space. The drawback of such a state with $\mathbf{P} = \mathbf{0}$ is a cost in the spin contribution (i.e., Zeeman energy) to the anisotropy energy in Eq. (4), because the amplitude of the spin magnetization $|\mathbf{S}|$ also vanishes according to the equation $|\mathbf{S}| = |\mathbf{P}| = |\cos\alpha|$ that is valid [13] for a generic CP^3 spinor. Therefore, this state can only be realized in the limit $\Delta_Z \to 0$. For finite Δ_Z, $u_z > 1/2$, and $u_\perp > 1/2$, energy optimization leads to states with *partially* entangled spin and pseudospin, with either easy-plane ($u_z > u_\perp$) or easy-axis character ($u_z < u_\perp$).

To compute the phase diagram of CP^3 Skyrmions with topological charge $\mathcal{Q} = 1$, we use that the by far largest contribution to the Skyrmion energy is given by the gradient term in Eq. (3). Minimizing this contribution, we obtain a Skyrmion with energy $E_{\mathrm{sk}} = 4\pi\rho_S$ of the form

$$Z_{\mathrm{skyr}}(x, y) = \mathcal{N}(r)^{-1}[(x + iy)F - \lambda(r)C], \tag{6}$$

with constant $\lambda(r) = \lambda_0$ and $r = |\mathbf{r}|$. F is the CP^3 spinor of the FM background described above, and $\mathcal{N}(r)$ ensures the normalization of $Z_{\mathrm{skyr}}(\mathbf{r})$. Because of the SU(4) symmetry and scale invariance of the gradient term, C can be chosen as an arbitrary spinor perpendicular to F, and also the size of the Skyrmion obtained from λ_0 is not fixed. These parameters are fixed by the remaining much smaller anisotropy terms and the Coulomb energy. While the anisotropy terms favor small Skyrmions, the Coulomb energy increases their size. For a quantitative analysis, one has to take into account that for a constant $\lambda(r) = \lambda_0$ the slow $1/r$ decay of the idealized SU(4) Skyrmion causes a logarithmic divergence of the anisotropy energies Eq. (4). To obtain the asymptotically exact Skyrmion energetics [2] and to avoid this divergency, it is sufficient to parametrize $\lambda(r) = \lambda_0 \exp(-r^2/\kappa\lambda_0^2)$. For each value of $u_\perp$ and u_z, we therefore minimize $\delta E = E[Z_{\mathrm{skyr}}(\mathbf{r})] - E[Z(\mathbf{r}) = F]$ using λ_0, κ and four variational angles characterizing C [20]. Typical Skyrmion sizes obtained from this optimization are on the order of 50–100 graphene lattice spacings for realistic parameters. Notice that this is much larger than shown in our figures, where we have used a smaller Skyrmion size that corresponds to unphysical magnetic fields ($B \sim 1000$ T). However, the patterns are simpler to visualize and can easily be upscaled to realistic sizes.

The resulting Skyrmion phases are shown in Fig. 2. Let us first concentrate on the rather simple cases $u_z \le 0$ or $u_\perp \le 0$, where the background F is a product state of a spin and a pseudospin FM. Either a spin or a pseudospin Skyrmion can be formed to accommodate the $\mathcal{Q} = 1$ topological charge. Charge excitations of minimal energy are mostly spin Skyrmions

$$Z_{\mathrm{spin}}(x, y) = \mathcal{N}(r)^{-1}\psi^P \otimes [(x + iy)\psi^S_\uparrow - \lambda(r)\psi^S_\downarrow], \tag{7}$$

where the spinors $\psi^S_\uparrow = (1, 0)^T$ and $\psi^S_\downarrow = (0, 1)^T$ represent the spin orientation and ψ^P is the (homogeneous) pseudospin component, which is unaffected by a pure spin texture. Generally, the spinors can be represented in terms of the the four angles θ_S, ϕ_S and θ_P, ϕ_P that describe the spin and pseudospin polarizations on their respective Bloch spheres, with

$$\begin{aligned}\psi^I &= [\cos(\theta_I/2), e^{i\phi_I}\sin(\theta_I/2)]^T,\\ \chi^I &= [-e^{-i\phi_I}\sin(\theta_I/2), \cos(\theta_I/2)]^T,\end{aligned} \tag{8}$$

for $I = S, P$. The spinors $\psi^S_\uparrow$ and $\psi^S_\downarrow$ in Eq. (7) correspond then to $\psi^S(\theta_S = 0)$ and $\chi^S(\theta_S = 0)$, respectively.

At $u_z \sim u_\perp$ and u_z, $u_\perp \le 1/2$, it becomes energetically favorable to form pseudospin instead of spin Skyrmions,

$$Z_{\mathrm{pseudospin}}(x, y) = \mathcal{N}(r)^{-1}[(x + iy)\psi^P - \lambda(r)\chi^P] \otimes \psi^S_\uparrow, \tag{9}$$

where we have $\theta_P = 0$ and $\theta_P = \pi/2$ in ψ^P, χ^P for the easy-axis pseudospin easy-plane pseudospin FM background, respectively. The pseudospin Skyrmion in an easy-axis pseudospin FM background is represented as a wrapping of the Bloch sphere in the inset of Fig. 1(a), as well as in a lattice-resolved image Fig. 1(a), for a set of parameters corresponding to point 3 in Fig. 2. While the CP^3 fields $Z(\mathbf{r})$ only provide an envelope function in a continuum description, the lattice-resolved patterns can be obtained by a convolution with Gaussian functions representing the atomic wave functions on the lattice sites [20]. The electronic density is concentrated on the A sublattice at the Skyrmion center $r = 0$, whereas solely the B sublattice is populated at $r \to \infty$. The situation is more involved for a pseudospin Skyrmion in an easy-plane pseudospin FM [Fig. 1(b), for parameters corresponding to point 2 in Fig. 2]. Since the pseudospin polarization is bound to the xy plane at $r = 0$ (gray arrow) and at $r \to \infty$ (orange arrow), both sublattices are equally populated there. However, because the pseudospin polarization explores all points of the Bloch sphere, the south pole at some point $\mathbf{r}_1$ and the north pole at $\mathbf{r}_2 = -\mathbf{r}_1$, this yields the double-core structure in the lattice-resolved density plot Fig. 1(b), where solely

the $A(B)$sublattice is populated at $\mathbf{r}_1(\mathbf{r}_2)$. This is reminiscent of bimerons in bilayer quantum Hall systems in GaAs heterostructures [17,18,25].

The predominance of pseudospin Skyrmions at $u_z \sim u_\perp$ is a consequence of a partial symmetry restoration at the transition $u_z = u_\perp$—the pseudospin component in Eq. (4) is then proportional to $u_z \mathbf{P} \cdot \mathbf{P}$, and all pseudospin orientations are equally possible. A deformation of the pseudospin texture thus becomes very soft, accompanied by no energy cost, while the full spin polarization allows one to minimize the Zeeman energy in Eq. (4). Similarly to spin Skyrmions with a vanishing Zeeman gap [2], the size of the pseudospin Skyrmion diverges, apart from a logarithmic correction, as $\lambda_0/l_B \sim (e^2/\epsilon l_B \Delta |u_z - u_\perp|)^{1/3}$, when approaching $u_z = u_\perp$ along line A in Fig. 2, as one may understand from a simple scaling analysis of the competing terms: while the pseudospin symmetry-breaking in Eq. (4) scales as $\sim \lambda_0^2 |u_\perp - u_z|$, the Coulomb interaction in Eq. (3) scales as $\sim e^2/\epsilon\lambda_0$.

The probably most exotic Skyrmion types are obtained for $u_z,\ u_\perp \geq 0$ (yellow in Fig. 2), where spin-pseudospin entanglement is energetically favored. A normalized CP^3 spinor is described by six angles. Whereas the first four have been introduced in Eq. (8), the remaining two (α, β) can be viewed as angles on a *third* Bloch sphere that describes the *entanglement* between spin and pseudospin [13]

$$\Psi = \cos\frac{\alpha}{2}\psi^P \otimes \psi^S + e^{i\beta}\sin\frac{\alpha}{2}\chi^P \otimes \chi^S. \qquad (10)$$

This allows us to define the *entanglement Skyrmion* as an SU(4) texture that fully covers the third (entanglement) Bloch sphere; see the insets of Fig. 3, where the north and south poles correspond to no entanglement. This Skyrmion can be formed both in an unentangled background [orange arrow pointing to the north pole in the inset of Fig. 3(a)] and in a FM background with nonzero entanglement; in the latter case, the arrow representing the spinor F points away from the poles [inset of Fig. 3(b)].

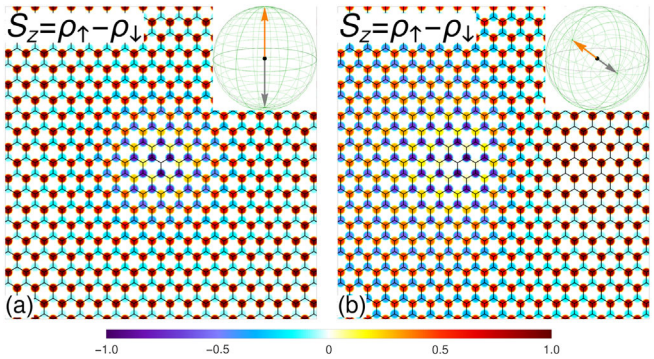

FIG. 3. Entanglement Skyrmions in an unentangled (a) and an entangled (b) FM background. The two subfigures sketch the lattice-resolved profiles of the z component of the spin magnetization S_z in a color plot (blue for spin-up and red for spin-down densities). Insets show the entanglement Bloch sphere spanned by α and β [see Eq. (10)]. In each Bloch sphere, the orange and gray arrows show the directions corresponding to the FM background and to the Skyrmion center, respectively. Panels (a) and (b) correspond to points 6 and 7 in Fig. 2, respectively.

As we have pointed out above, the fingerprint of entanglement is a locally antiferromagnetic pattern, and entanglement is thus better visible in a lattice-resolved plot of the spin magnetization rather than in plots of the different spin densities (such as in Fig. 1). We therefore plot $S_z = \rho_\uparrow - \rho_\downarrow$ in Fig. 3 for the profile of entanglement Skyrmions. (The separate patterns for $\rho_\uparrow$ and $\rho_\downarrow$ for the same Skyrmion types can be found in Ref. [20].) Figure 3(a) corresponds to the entanglement Skyrmion in an unentangled FM background (point 6 in Fig. 2). We notice that also the Skyrmion center is unentangled, with all electrons on a single sublattice. In contrast to a pseudospin Skyrmion in an easy-axis pseudospin FM background, it is maximally entangled at $r \sim \lambda_0$, where one notices the above-mentioned antiferromagnetic pattern, with all spin-up electrons on the B and all spin-down electrons on the A sublattice. Figure 3(b), which represents the entanglement Skyrmion in an *entangled* FM background (point 7 in Fig. 2), shows again a double-core structure. The two cores correspond to regions where $Z(r)$ has no entanglement, while the entangled FM background is manifest in the antiferromagnetic pattern. Finally, we notice that one obtains again pseudospin Skyrmions at $u_z \sim u_\perp$, $u_z,\ u_\perp > 1/2$ (upper-right region in Fig. 2). However, to minimize the symmetry-breaking terms, they are partially entangled, i.e., the polarization explores regions of the entanglement Bloch sphere different from the poles. Hence, the modulus $|\cos\alpha|$ of the pseudospin polarization is decreased ("deflated pseudospin Skyrmion" in Fig. 2), and the density contrast would be reduced as compared to Fig. 1.

In conclusion, we have investigated different Skyrmion types in graphene at $\nu = \pm 1$. Apart from the usual spin Skyrmion, the valley pseudospin analogue yields distinctive charge patterns on the graphene lattice because valley and sublattice degrees of freedom are identical in the $n = 0$ LL. Graphene is therefore an ideal system to probe Skyrmions with a valley pseudospin texture. This can, in principle, be achieved in lattice-resolved STS in the energy range corresponding to $n = 0$. Since quantum-Hall Skyrmions carry, in contrast to those in chiral magnets, electric charge, their density can be controlled by a back gate and one can thus achieve the limit of few isolated Skyrmions. Most saliently, the large SU(4) symmetry of the leading terms in the nonlinear sigma model yields exotic entanglement Skyrmions stabilized for positive values of the parameters u_z and $u_\perp$. These topological objects also have a clear fingerprint in the form of *antiferromagnetic* patterns, e.g., in spin-resolved STS, even if they are manifestations of SU(4)-FM states. Our results show that using STS with a magnetic tip, one can not only detect but

also identify the various Skyrmion types and analyze their size as a function of B [2,20]. Notice that the relative weight of the parameters can to some extent be tuned by the B field and its orientation—while the Zeeman energy depends on the total field, the pseudospin couplings only depend on its perpendicular component [21,22]. If one, furthermore, combines magnetic tips with different orientations of the magnetization [26] one can actually map out locally 5 of the 6 angles parametrizing the CP^3 field [see Eq. (10)]. Only the $\beta - \phi_P$ combination cannot be measured directly. While we have concentrated the discussion on Skyrmions with topological charge $\mathcal{Q} = 1$, in topological sectors with higher charge the Coulomb repulsion is likely to break up a single charge $\mathcal{Q}$ into several charge-1 Skyrmions that are eventually arranged into a lattice [7,27].

We acknowledge fruitful discussions with Markus Morgenstern. Y. L. is funded by the China Scholarship Council.

[1] T. H. R. Skyrme, Proc. R. Soc. A **260**, 127 (1961).
[2] S. L. Sondhi, A. Karlhede, S. A. Kivelson, and E. H. Rezayi, Phys. Rev. B **47**, 16419 (1993).
[3] A. H. Castro Neto, F. Guinea, N. M. R. Peres, K. S. Novoselov, and A. K. Geim, Rev. Mod. Phys. **81**, 109 (2009).
[4] M. O. Goerbig, Rev. Mod. Phys. **83**, 1193 (2011).
[5] S. E. Barrett, G. Dabbagh, L. N. Pfeiffer, K. W. West, and R. Tycko, Phys. Rev. Lett. **74**, 5112 (1995).
[6] N. Nagaosa and Y. Tokura, Nat. Nanotechnol. **8**, 899 (2013).
[7] S. Mühlbauer, B. Binz, F. Jonietz, C. Pfleiderer, A. Rosch, A. Neubauer, R. Georgii, and P. Böni, Science **323**, 915 (2009).
[8] N. Romming, C. Hanneken, M. Menzel, J. E. Bickel, B. Wolter, K. von Bergmann, A. Kubetzka, and R. Wiesendanger, Science **341**, 636 (2013).
[9] T. Schulz, R. Ritz, A. Bauer, M. Halder, M. Wagner, C. Franz, C. Pfleiderer, K. Everschor, M. Garst, and A. Rosch, Nat. Phys. **8**, 301 (2012).
[10] F. Freimuth, R. Bamler, Y. Mokrousov, and A. Rosch, Phys. Rev. B **88**, 214409 (2013).
[11] K. Nomura and A. H. MacDonald, Phys. Rev. Lett. **96**, 256602 (2006); K. Yang, S. Das Sarma, and A. H. MacDonald, Phys. Rev. B **74**, 075423 (2006).
[12] M. O. Goerbig, R. Moessner, and B. Douçot, Phys. Rev. B **74**, 161407 (2006); J. Alicea and M. P. A. Fisher, Phys. Rev. B **74**, 075422 (2006).
[13] B. Douçot, M. O. Goerbig, P. Lederer, and R. Moessner, Phys. Rev. B **78**, 195327 (2008).
[14] Y. P. Shkolnikov, S. Misra, N. C. Bishop, E. P. De Poortere, and M. Shayegan, Phys. Rev. Lett. **95**, 066809 (2005).
[15] D. P. Arovas, A. Karlhede, and D. Lilliehöök, Phys. Rev. B **59**, 13147 (1999); B. Douçot, D. Kovrizhin, and R. Moessner, Phys. Rev. B **93**, 094426 (2016).
[16] *The Multifaceted Skyrmion*, edited by G. E. Brown and M. Rho (World Scientific, Singapore, 2014).
[17] S. M. Girvin, *The Quantum Hall Effect: Novel Excitations and Broken Symmetries, Topological Aspects of Low-Dimensional Systems—Ecole d'Ete de Physique Théorique LXIX*, edited by A. Comptet, T. Jolicoeur, S. Ouvry, and F. David (Springer, New York, 1999); Z. F. Ezawa, *Quantum Hall Effects: Field Theoretical Approach and Related Topics* (World Scientific, Singapore, 2000).
[18] K. Moon, H. Mori, K. Yang, S. M. Girvin, A. H. MacDonald, I. Zheng, D. Yoshioka, and S.-C. Zhang, Phys. Rev. B **51**, 5138 (1995).
[19] Z. F. Ezawa, Phys. Rev. Lett. **82**, 3512 (1999).
[20] See Supplemental Material at http://link.aps.org/supplemental/10.1103/PhysRevLett.117.056806 for more details about the effective model and energy calculations.
[21] J.-N. Fuchs and P. Lederer, Phys. Rev. Lett. **98**, 016803 (2007).
[22] K. Nomura, S. Ryu, and D.-H. Lee, Phys. Rev. Lett. **103**, 216801 (2009); C.-Y. Hou, C. Chamon, and C. Mudry, Phys. Rev. B **81**, 075427 (2010).
[23] I. F. Herbut, Phys. Rev. B **75**, 165411 (2007); **76**, 085432 (2007).
[24] M. Kharitonov, Phys. Rev. B **85**, 155439 (2012).
[25] L. Brey, H. A. Fertig, R. Cote, and A. H. MacDonald, Phys. Rev. B **54**, 16888 (1996).
[26] S. Heinze, K. von Bergmann, M. Menzel, J. Brede, A. Kubetzka, R. Wiesendanger, G. Bihlmayer, and S. Blügel, Nat. Phys. **7**, 713 (2011).
[27] R. Côté, D. B. Boisvert, J. Bourassa, M. Boissonneault, and H. A. Fertig, Phys. Rev. B **76**, 125320 (2007); R. Côté, J.-F. Jobidon, and H. Fertig, *ibid.* **78**, 085309 (2008); X. Z. Yu, Y. Onose, N. Kanazawa, J. H. Park, J. H. Han, Y. Matsui, N. Nagaosa, and Y. Tokura, Nature (London) **465**, 901 (2010); J. H. Han, J. Zang, Z. Yang, J.-H. Park, and N. Nagaosa, Phys. Rev. B **82**, 094429 (2010); D. L. Kovrizhin, B. Douçot, and R. Moessner, Phys. Rev. Lett. **110**, 186802 (2013).